optica

Mid-infrared laser filaments in air at a kilohertz repetition rate

Houkun Liang,[1] Darshana L. Weerawarne,[2] Peter Krogen,[1] Rostislav I. Grynko,[2] Chien-Jen Lai,[1] Bonggu Shim,[2] Franz X. Kärtner,[1,3,4] and Kyung-Han Hong[1,*]

[1]Research Laboratory of Electronics, Massachusetts Institute of Technology (MIT), Cambridge, Massachusetts 02139, USA
[2]Department of Physics, Applied Physics & Astronomy, Binghamton University, State University of New York, Binghamton, New York 13902, USA
[3]Center for Free-Electron Laser Science, DESY and Department of Physics, University of Hamburg, Hamburg, Germany
[4]The Hamburg Center for Ultrafast Imaging, Luruper Chaussee 149, 22761 Hamburg, Germany
*Corresponding author: kyunghan@mit.edu

Received 4 January 2016; revised 26 May 2016; accepted 27 May 2016 (Doc. ID 256503); published 21 June 2016

Laser filamentation overcomes diffraction over a highly extended distance, making itself a powerful tool for long-range stand-off detection and light detection and ranging (LIDAR) applications. Mid-infrared (mid-IR) wavelengths are optimal for detecting biochemicals and air pollutants due to molecular fingerprints. Here, we demonstrate mid-IR laser filamentations in ambient air at a kilohertz repetition rate for the first time. Laser filaments significantly longer than the linear confocal parameter are generated with a pump power exceeding the critical power in air using a kilohertz, 2.1 μm, femtosecond, multi-millijoule optical parametric chirped-pulse amplifier. Odd-harmonic generation up to the ninth order at ultraviolet and the mid-IR spectral extensions up to 3.5 μm are observed. The highest third and fifth harmonic efficiencies from ambient air are obtained, to our knowledge, thanks to the extended interaction length within the filaments. Numerical simulations reproduce the harmonic generation with good agreement and confirm that the plasma effect dominates over the higher-order Kerr effect as the main defocusing mechanism of laser filamentation in our experiment. The detection of atmospheric CO_2 is demonstrated via mid-IR absorption spectroscopy. High-flux ultrabroadband mid-IR filaments are useful for the fast and sensitive detection of multiple chemical species in air.

OCIS codes: (320.6629) Supercontinuum generation; (190.0190) Nonlinear optics; (300.6340) Spectroscopy, infrared.

http://dx.doi.org/10.1364/OPTICA.3.000678

Laser filamentation is a highly nonlinear process that occurs as the self-focusing from the optical Kerr effect is balanced by diffraction, plasma defocusing, and other nonlinear mechanisms. The laser peak power needs to be higher than the critical power that scales with λ^2 to reach the filamentation regime, where λ is the laser wavelength. Filamentation has been widely studied in solids and high-pressure gases for various applications, such as supercontinuum generation, few-cycle pulse compression, and high-harmonic generation [1,2]. Filamentation in air has especially attracted considerable attention for applications in remote sensing, LIDAR, and laser-induced breakdown spectroscopy [3,4]. Compared to the traditional LIDAR and spectroscopy based on linear laser beam propagation, filamentation overcomes diffraction over much longer distances, and, additionally, the back scattered light is much more directional [2]. This makes laser filamentation a powerful tool for long-range stand-off detection. Moreover, the broadband supercontinuum from the filamentation covers a large spectral range, enabling us to access multiple single-wavelength traces simultaneously in a single-shot measurement. However, most experimental work on filamentation in ambient air has been limited to the visible and near-infrared (near-IR) range, where high-energy, ultrafast laser sources are readily available. By extending the spectral range to the mid-IR, one could explore higher-order nonlinear processes, as the odd harmonics in the visible and near-IR regions propagate well in the atmosphere through filaments [5–7]. More importantly, mid-IR filamentation in air is highly useful in the direct detection of biochemicals and air pollutants with the resonant fingerprints of the common molecules, such as H_2O, CO_2, CO, and NH_4.

Even though there have been several reports on odd-harmonic generation in air pumped by ~2 μm optical parametric amplifiers in the tight focusing regime [8,9] to determine whether plasma (standard model [10]) or the higher-order Kerr effect (HOKE) [11,12] is dominant in laser filamentation, the first and sole demonstration of mid-IR filamentation in air, pumped by a 3.9 μm optical parametric chirped-pulse amplifier (OPCPA), was reported very recently [5,6]. However, the mid-IR filaments were generated at a low repetition rate of 20 Hz, limited by the laser source. Increasing the repetition rate to the kilohertz range would give orders of magnitude higher photon flux and data acquisition rate, which is highly favorable for practical applications like remote sensing. Furthermore, ~2 μm of wavelength is of great interest due to the recent advancement of Ho- and Tm-doped amplifiers suitable for compact high-power, ultrafast mid-IR sources [13].

In this Letter, we report on the demonstration of mid-IR filamentation in air, for the first time, at a kilohertz repetition rate, pumped by a kilohertz, multi-millojoule, 2.1 μm OPCPA. The

odd harmonic generation is observed up to ninth order at 230 nm. The maximum efficiencies of the third (TH), fifth (FiH), and seventh (SVH) harmonics are measured to be $\sim 5 \times 10^{-3}$, $\sim 1.5 \times 10^{-4}$, and $\sim 5 \times 10^{-6}$, respectively. Numerical simulations based on coupled nonlinear Schrödinger equations (NLSE) show a quantitative agreement with the experimental harmonic generation and confirm that the plasma defocusing is the main defocusing mechanism in the self-guiding rather than the HOKE in our experiment. On the mid-IR side, the supercontinuum is extended to 3.5 μm with loose focusing geometry. By making use of the mid-IR filamentation in air with a kilohertz repetition rate, we detect atmospheric CO_2 with a high sensitivity via mid-IR absorption spectroscopy.

In the experiment, 2.1 μm, 1.7 mJ, 33 fs pulses at a 1 kHz repetition rate are delivered from a three-stage OPCPA pumped by a cryogenic Yb:YAG chirped-pulse amplifier [14,15]. The peak power of ~52 GW exceeds the ~45 GW critical power of self-focusing at 2.1 μm wavelength in ambient air [5]. The OPCPA is capable of generating up to 3.5 mJ (>100 GW). CaF_2 lenses with focal lengths ranging from 100 to 1000 mm are used to focus the beam with an input diameter of ~10 mm ($1/e^2$) in air. The experimental schematics are illustrated in Figs. S1–S4 of the Supplement 1.

Single laser filaments are formed in air, as shown in Fig. 1(a). For example, a-few-centimeter-long plasma column is observed with an $f = 300$ mm lens, where the confocal range without filamentation is only ~4.6 mm for a diffraction-limited Gaussian beam waist of ~40 μm, clearly indicating the formation of a filament. The focused beam size is actually ~51 μm, with M^2 of ~1.65 having the same confocal range. The length of filament is as long as 10 cm for $f = 1000$ mm. The spectrum of the filament from ultraviolet (UV) to the mid-IR is measured with three different spectrometers (Thorlabs CCS series, Ocean Optics USB2000, and a Horiba scanning monochromator). The measured overall spectrum with $f = 300$ mm is shown in Fig. 1(b). Dramatic spectral extension from the mid-IR to UV occurs with the filamentation. Odd harmonics up to ninth harmonic (NH) are generated, corresponding to a spectral extension to 230 nm. At the same time, an octave-spanning supercontinuum (1.5–3.0 μm) is generated on the mid-IR side.

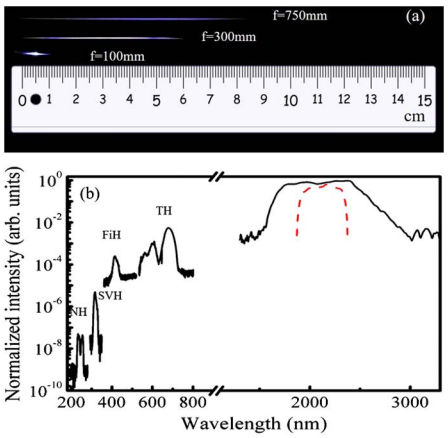

Fig. 1. (a) Photographs of the filaments formed in air focused using CaF_2 lenses with $f = 750$, 300, and 100 mm, (b) the supercontinuum and odd-harmonic spectra generated by filaments with $f = 300$ mm. The red dashed curve is the initial spectrum from our 2.1 μm OPCPA. The wavelength axis in the mid-IR is scaled to the half of the visible.

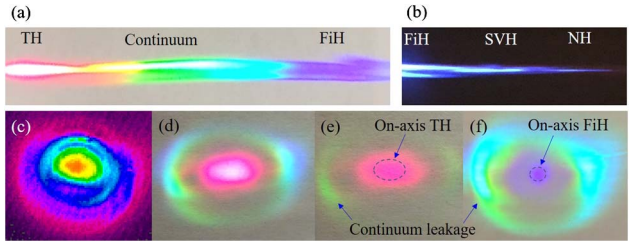

Fig. 2. (a) and (b) show the far-field images of the individual harmonics from a filament, diffracted by a grating. The far-field images of (c) fundamental, (d) overall-visible, (e) TH, and (f) FiH radiation. There is green and cyan continuum leakage in (e) and (f), respectively, due to the finite bandwidth of the color filters used.

Figures 2(a) and 2(b) show the far-field image of the filament diffracted by a grating. Bright TH and visible continuum, blue FiH, as well as spatially separated UV fluorescence spots that correspond to the SVH and NH are observed. It is interesting to find that the far-field patterns of TH and FiH as well as the visible continuum are composed of a bright center line and two separated emission lines, which indicates a conical profile, while the SVH and the NH tend to be on-axis, as shown in Fig. 2(b). The far-field profiles of the fundamental, overall-visible, TH, and FiH radiation are measured with color filters, as shown in Figs. 2(c)–2(f). Figures 2(d)–2(f) present the real color on a paper sheet, while Fig. 2(c) in pseudo-color is directly measured on a pyroelectric camera and therefore has a horizontally flipped image. A conical pattern is observed for all the four far-field profiles. Compared to TH in Fig. 2(e), FiH in Fig. 2(f) has a more concentrated on-axis component and a well-separated off-axis emission, indicating the transition toward the on-axial emission as the harmonic order increases. It is also possible that these off-axis emissions are attributed to the conical emission of the fundamental beam.

The conversion efficiencies of TH, FiH, and SVH with different focal length lenses are measured using a 600 groove/mm grating with a known diffraction efficiency and a power meter (see Fig. S2 of Supplement 1). Color filters and apertures are used to filter out the scattered light. As shown in Fig. 3(a), the maximum harmonic efficiencies have been obtained at $f = 250$–350 mm, with 1.7 mJ of energy. At long and short focal lengths, such as 750 and 100 mm, the harmonic efficiencies drop because both the intensity and the interaction length are important for the harmonic generation. The optimal focusing geometry provides the balance between a high peak intensity and a long interaction length extended by filamentation. The energy loss, depletion of neutral atoms, and phase mismatch induced by ionization are also responsible for the drop of harmonic generation efficiencies at

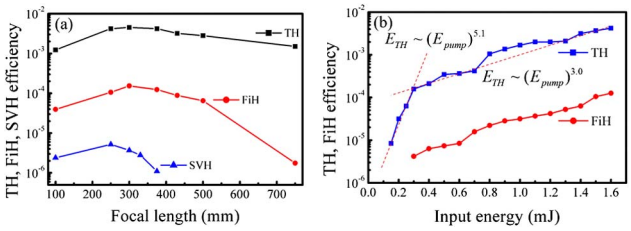

Fig. 3. (a) The measured TH, FiH, and SVH efficiencies from the filamentation in air, using 1.7 mJ pump energy and different focal length lenses. (b) The measured TH and FiH efficiencies with an $f = 330$ mm lens at different pump energies.

very tight focus. The maximum efficiencies of TH, FiH, and SVH are measured as $\sim 5 \times 10^{-3}$, $\sim 1.5 \times 10^{-4}$, and $\sim 5 \times 10^{-6}$, respectively. To our best knowledge, these are the highest reported TH and FiH efficiencies from ambient air.

We also measured the TH and FiH efficiencies versus the pump energy with a focal length of 330 mm, as shown in Fig. 3(b). The detector assisted with a lock-in amplifier is used to exclude the thermal noise for detecting weak signals. It is observed that the efficiency of TH exhibits a dramatic increase with the slope dependence of energy measured as $E_{\mathrm{TH}} \sim (E_{\mathrm{pump}})^{5.1}$ up to 0.3 mJ, which is attributed mainly to self-focusing and consistent with previous reports with air or long gas cells [16] using near-IR lasers. The estimated nominal pump intensity at 0.3 mJ is $\sim$200 TW/cm^2, where the nominal pump intensity is the peak intensity in vacuum. As the pump energy increases beyond the saturation intensity of oxygen and nitrogen, the air becomes substantially ionized and the intensity clamping occurs due to the plasma defocusing and filamentation. The peak intensity in the filament does not exceed 100 TW/cm^2 due to intensity clamping, as shown by the calculation in Fig. 4(c). However, the extended interaction length, channeled by the filamentation, and the partially compensated Guoy phase shift keep the TH efficiency increasing. As a result, the growth of TH is slowed down with $E_{\mathrm{TH}} \sim (E_{\mathrm{pump}})^{3.0}$. The TH conversion efficiency of $\sim 5 \times 10^{-3}$ is obtained at 1.7 mJ. For the FiH generation, as shown in Fig. 3(b), measurable FiH appears at 0.3 mJ of input energy when the TH efficiency reaches $>10^{-4}$. The FiH efficiency of $\sim 1.5 \times 10^{-4}$ is obtained at 1.7 mJ. The FiH efficiency also follows the slope of $\sim (E_{\mathrm{pump}})^{3.0}$ due to the filament with the clamped intensity.

We also numerically calculated the harmonic generation efficiency using a wave propagation model based on the coupled NLSE [17–19] (see Supplement 1 for details), which accounts for the presence of the fundamental and harmonic fields up to NH. We consider relevant nonlinear interactions and their effects on harmonic generation. In particular, we model the effects of self-phase modulation (SPM) and cross-phase modulation (XPM) on phase mismatch between the fundamental and the generated harmonic fields. Our model considers diffraction, dispersion, group velocity walk-off, ionization absorption, plasma absorption and defocusing, and SPM/XPM on beam propagation. FiH is generated via a direct process and a cascaded process involving the fundamental and generated harmonics (see Supplement 1 and Ref. [19] for details). For simplicity, we only consider the direct contributions arising from the nonlinearity coefficients n_6 and n_8 to SVH and NH generation. We ignore SPM and XPM by the weak harmonic fields. For the plasma generation, the Perelemov, Popov, and Terent'ev model [20] is used for the ionization of oxygen and nitrogen by the fundamental field. We ignore the Raman nonlinearity in our simulation mainly due to relatively short pulse duration and filament length (see Fig. S6 in Supplement 1).

We simulate the experimental condition with an $f = 300$ mm focusing geometry, which corresponds to a 40 μm $1/e^2$ beam radius at the focus, and we assume an index of refraction of air at 2.1 μm, as reported in Ref. [21]. The experimental beam size is $\sim$51 μm with M^2 of 1.65, but the difference in the simulation results between two beam sizes is almost negligible. We consistently use 40 μm to keep the same confocal range as in the experiment. In all of the following simulations, harmonic signals are calculated at a 100 mm propagation distance beyond the geometric focus. Gaussian profiles are used in both the time and space domains. Nonlinear refractive index coefficients are chosen based on those reported in Refs. [11,22]. The set of nonlinear index coefficients used is $n_2 = 1.2 \times 10^{-19}$ cm^2/W, $n_6 = 2.1 \times 10^{-46}$ cm^6/W^3, and $n_8 = -0.8 \times 10^{-59}$ cm^8/W^4. Comparative simulations are run by varying n_4 as a free parameter to match the experiments. In the simulations, n_2 and n_4 contribute to both the harmonic generation and SPM/XPM, while n_6 and n_8 only contribute to the harmonic generation. We also study the effect of higher-order nonlinearities on beam propagation by incorporating HOKE contributions in the phase modulation terms of the equations, thus simulating the HOKE model [12,21].

Figures 4(a) and 4(b) show the TH and FiH simulation results, respectively, for harmonic efficiency calculated with different nonlinearity coefficients. For all models, the saturation of the TH efficiency is reproduced by the simulation as the pump energy increases beyond 0.1 mJ. The efficiencies at 1.5 mJ, calculated from the standard model with $n_4 = 0$, are 6×10^{-3}, 2×10^{-4}, and 4×10^{-5} for TH, FiH, and SVH (see Fig. S7 in Supplement 1), respectively. The corresponding peak intensities are plotted in Fig. 4(c) along with the nominal pump intensity, showing the intensity clamping at $<$100 TW/cm^2. The plasma density in the filament is (6–9) $\times 10^{16}$ cm^{-3} for all the models. The standard model shows a good agreement with our experiment for TH and FiH efficiencies. Therefore, the models with SPM/XPM nonlinearity accounted for only up to n_4 predict harmonic efficiencies comparable to those measured experimentally. It should be noted that the HOKE model predicts harmonic efficiencies of TH and FiH considerably higher than those measured in the experiments, indicating that defocusing via plasma generation is more important than the HOKE in our experiment. While the standard model overestimates the SVH efficiency, the HOKE model has resulted in larger discrepancy in SVH calculations (see Fig. S7 in Supplement 1). The simulated spatial profiles of the fundamental beam and the harmonic beams qualitatively reproduce the experimental observations of ring patterns (see Fig. S8 in Supplement 1). We also provide the simulations based on the carrier-resolved unidirectional pulse propagation equation [23] in Figs. S9–S11 of Supplement 1 to further back up the coupled

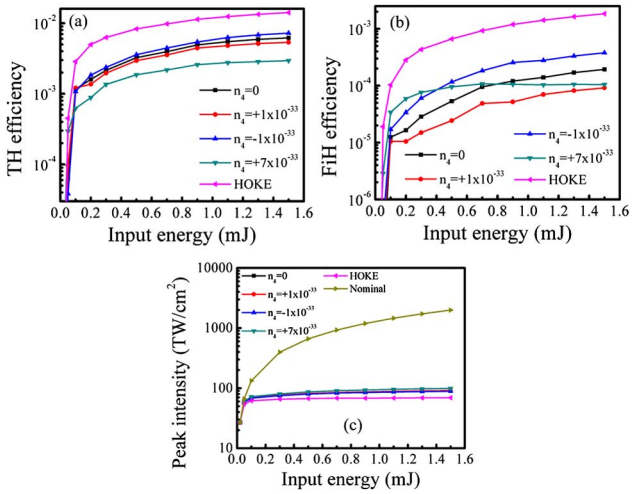

Fig. 4. Calculated efficiency of (a) TH and (b) FiH for different simulation models with $f = 300$ mm. The standard model with $n_4 = 0$, $+1 \times 10^{-33}$ cm^4/W^2, -1×10^{-33} cm^4/W^2, and $+7 \times 10^{-33}$ cm^4/W^2, and HOKE model are used. (c) The peak intensities versus input energy calculated for different models are compared to the nominal pump intensity.

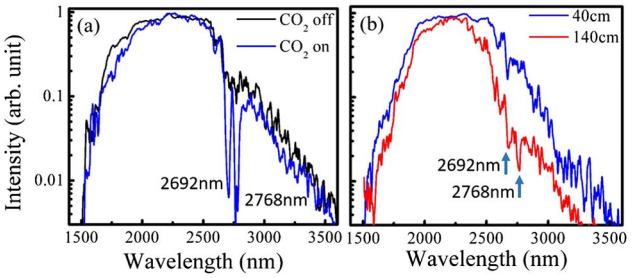

Fig. 5. (a) Comparison of the mid-IR continuum spectra after propagating through a CO_2 gas cell with gas turned on and off. (b) The mid-IR spectra with free propagation in air over 40 and 140 cm.

NLSE simulation results that lack the accurate calculation of continuum generation.

Finally, we demonstrate the mid-IR absorption spectroscopy of atmospheric CO_2 [24], a major greenhouse gas, to show the potential application to the sensitive detection of chemicals in air. A looser focus is found to enable a deeper extension to the mid-IR (see Fig. S5 in Supplement 1) because the spectral broadening is dominated by SPM of neutral atoms, which symmetrically extends the spectrum to both sides [25] with the minimal self-steepening and/or plasma effect. With $f = 1000$ mm, the supercontinuum from the mid-IR filament reaches 3500 nm, which is used in the experiment for absorption spectroscopy.

We check the absorption lines of CO_2 by letting the supercontinuum of the mid-IR filament propagate through a 300 mm-long gas cell filled with CO_2 at ~340 mbar (see Fig. S3 of Supplement 1 for the setup). The mid-IR spectra with CO_2 being turned on and off are compared in Fig. 5(a). Two distinct absorption lines of CO_2 at 2692 and 2768 nm are clearly recorded. The nearby water absorption lines are well separated. Then, we measure the mid-IR absorption spectra from the filament in the air with different propagation distances to detect the atmospheric CO_2 in the laboratory environment (~40% of humidity and 68°F of temperature). As shown in Fig. 5(b), CO_2 fingerprints are present and become outstanding as the propagation distance increases from 40 to 140 cm. This demonstrates that the direct absorption spectroscopy using the kilohertz, mid-IR filaments provides sufficient sensitivity to detect atmospheric CO_2 which composes only ~400 ppm in air. Compared to the existing laser filament-based remote sensing techniques, mid-IR absorption spectroscopy detects the molecules directly, instead of using fluorescence from the dissociated molecules (filament-induced nonlinear fluorescence spectroscopy) or laser-produced plasmas (filament-induced breakdown spectroscopy) [4]. (See Supplement 1 for other methods.) Therefore, mid-IR absorption spectroscopy via filamentation is expected to have better accuracy and reliability without the need for a post-data analysis. Ultrabroadband mid-IR filaments can also detect multiple molecular species at once.

In conclusion, we demonstrate the mid-IR filamentation in air at a kilohertz repetition rate, pumped at 2.1 μm, and the efficient odd harmonic generation up to NH. Our numerical study confirms that plasma effect dominates over HOKE as the main defocusing mechanism in the experiment. Direct absorption spectroscopy of atmospheric CO_2 is demonstrated. High-repetition-rate mid-IR filaments are useful tool for the sensitive detection of various chemicals in the atmosphere. Significant elongation of the filament length with energy scaling of mid-IR pump sources as well as backscattered light measurements will be needed for practical applications outside laboratories.

Funding. AFOSR (FA9550-12-1-0499, FA9550-14-1-0255); SUNY Research Foundation; SIMTech (SIMT/14-110023); A*STAR; Deutsche Forschungsgemeinschaft (DFG).

Acknowledgment. H. L. acknowledges the financial support from SIMTech (SIMT/14-110023) and A*STAR. P. K. acknowledges support from a NDSEG Graduate Fellowship. F. X. K. acknowledges support through the CFEL at DESY and the excellence cluster "The Hamburg Centre for Ultrafast Imaging- Structure, Dynamics and Control of Matter at the Atomic Scale" of the Deutsche Forschungsgemeinschaft.

See Supplement 1 for supporting content.

REFERENCES

1. A. Couairon and A. Mysyrowicz, Phys. Rep. **441**, 47 (2007).
2. L. Bergé, S. Skupin, R. Nuter, J. Kasparian, and J.-P. Wolf, Rep. Prog. Phys. **70**, 1633 (2007).
3. J. Kasparian, M. Rodriguez, G. Méjean, J. Yu, E. Salmon, H. Wille, R. Bourayou, S. Frey, Y.-B. André, A. Mysyrowicz, R. Sauerbrey, J.-P. Wolf, and L. Wöste, Science **301**, 61 (2003).
4. S. L. Chin, H. L. Xu, Q. Luo, F. Théberge, W. Liu, J. F. Daigle, Y. Kamali, P. T. Simard, J. Bernhardt, S. A. Hosseini, M. Sharifi, G. Méjean, A. Azarm, C. Marceau, O. Kosareva, V. P. Kandidov, N. Aközbek, A. Becker, G. Roy, P. Mathieu, J. R. Simard, M. Châteauneuf, and J. Dubois, Appl. Phys. B **95**, 1 (2009).
5. A. V. Mitrofanov, A. A. Voronin, D. A. Sidorov-Biryukov, A. Pugžlys, E. A. Stepanov, G. Andriukaitis, T. Flöry, S. Ališauskas, A. B. Fedotov, A. Baltuška, and A. M. Zheltikov, Sci. Rep. **5**, 8368 (2015).
6. A. V. Mitrofanov, A. A. Voronin, S. I. Mitryukovskiy, D. A. Sidorov-Biryukov, A. Pugžlys, G. Andriukaitis, T. Flöry, E. A. Stepanov, A. B. Fedotov, A. Baltuška, and A. M. Zheltikov, Opt. Lett. **40**, 2068 (2015).
7. P. Panagiotopoulos, P. Whalen, M. Kolesik, and J. V. Moloney, Nat. Photonics **9**, 543 (2015).
8. G. O. Ariunbold, P. Polynkin, and J. V. Moloney Ariunbold, Opt. Express **20**, 1662 (2012).
9. A. Nath, J. A. Dharmadhikari, A. K. Dharmadhikari, and D. Mathur, Opt. Lett. **38**, 2560 (2013).
10. M. Kolesik, E. M. Wright, and J. V. Moloney, Opt. Lett. **35**, 2550 (2010).
11. V. Loriot, E. Hertz, O. Faucher, and B. Lavorel, Opt. Express **18**, 3011 (2010).
12. P. Béjot, J. Kasparian, S. Henin, V. Loriot, T. Vieillard, E. Hertz, O. Faucher, B. Lavorel, and J.-P. Wolf, Phys. Rev. Lett. **104**, 103903 (2010).
13. A. Dergachev, Proc. SPIE **8599**, 85990B (2013).
14. C.-L. Chang, P. Krogen, K.-H. Hong, L. E. Zapata, J. Moses, A.-L. Calendron, H. K. Liang, C.-J. Lai, G. J. Stein, P. D. Keathley, G. Laurent, and F. X. Kärtner, Opt. Express **23**, 10131 (2015).
15. K.-H. Hong, C.-J. Lai, J. P. Siqueira, P. Krogen, J. Moses, C.-L. Chang, G. J. Stein, L. E. Zapata, and F. X. Kärtner, Opt. Lett. **39**, 3145 (2014).
16. R. A. Ganeev, M. Suzuki, M. Baba, H. Kuroda, and I. A. Kulagin, Appl. Opt. **45**, 748 (2006).
17. N. Aközbek, A. Iwasaki, A. Becker, M. Scalora, S. L. Chin, and C. M. Bowden, Phys. Rev. Lett. **89**, 143901 (2002).
18. Y. Liu, M. Durand, A. Houard, B. Forestier, A. Couairon, and A. Mysyrowicz, Opt. Commun. **284**, 4706 (2011).
19. D. L. Weerawarne, X. Gao, A. L. Gaeta, and B. Shim, Phys. Rev. Lett. **114**, 093901 (2015).
20. A. M. Perelemov, V. S. Popov, and M. V. Terent'ev, Sov. Phys. J. Exp. Theor. Phys. **23**, 924 (1966).
21. R. J. Mathar, J. Opt. A **9**, 470 (2007).
22. D. Wang and Y. Leng, Opt. Commun. **328**, 41 (2014).
23. M. Kolesik, J. V. Moloney, and M. Mlejnek, Phys. Rev. Lett. **89**, 283902 (2002).
24. T. Somekawa, M. Fujita, and Y. Izawa, Appl. Phys. Express **3**, 082401 (2010).
25. K. Lim, M. Durand, M. Baudelet, and M. Richardson, Sci. Rep. **4**, 7217 (2014).